ASTM INTERNATIONAL
Standards Worldwide

Materials Performance and Characterization

Yan Li,[1] D. L. McDowell,[1] and Min Zhou[1]

DOI: 10.1520/MPC20130064

A Multiscale Framework for Predicting Fracture Toughness of Polycrystalline Metals

VOL. 3 / NO. 3 / 2014

Materials Performance and Characterization

doi:10.1520/MPC20130064 / Vol. 3 / No. 3 / 2014 / available online at www.astm.org

Yan Li,[1] D. L. McDowell,[1] and Min Zhou[1]

A Multiscale Framework for Predicting Fracture Toughness of Polycrystalline Metals

Reference

Li, Yan, McDowell, D. L., and Zhou, Min, "A Multiscale Framework for Predicting Fracture Toughness of Polycrystalline Metals," *Materials Performance and Characterization*, Vol. 3, No. 3, 2014, pp. 157–172, doi:10.1520/MPC20130064. ISSN 2165-3992

ABSTRACT

Microstructure has a strong influence on fracture toughness of materials through the activation of different fracture mechanisms. To tailor the fracture resistance through microstructure design, it is important to establish relations between microstructure and fracture toughness. A multiscale computational framework based on the Cohesive Finite Element Method (CFEM) is introduced to facilitate relations between microstructure and the fracture toughness of ductile polycrystalline materials. This material design framework includes 3D image based microstructure reconstruction, 3D meshing, and finite element implementation. It allows the material fracture toughness to be predicted through explicit simulation of fracture processes involving arbitrary crack paths, crack tip microcracking, and branching. Cohesive elements are embedded both within the grains and along the grain boundaries to resolve the different material separation processes. The calculations carried out concern Ti-6Al-4V alloy and focused on the two primary fracture mechanisms which are correlated with microstructure characteristics, constituent properties, and deformation behaviors. The methodology is potentially useful for both the selection of materials and tailoring of microstructure to improve fracture resistance.

Keywords

multiscale framework, cohesive finite element method, crystal plasticity, microstructure-fracture toughness

Manuscript received October 1, 2013; accepted for publication January 3, 2014; published online March 26, 2014.

[1] The George W. Woodruff School of Mechanical Engineering School of Material Science and Engineering, Georgia Institute of Technology, Atlanta, GA 30332-0405.

[2] This paper is a contribution to a Special Issue of *Materials Performance and Characterization* on "Fracture Toughness," Guest Editors, Bojan Podgornik and Votjeh Leskovsek, Institute of Metals and Technology, Ljubljana, Slovenia.

Introduction

The development of new and improved materials with specified performance requirements requires in-depth understanding of the microstructure-property relationships. To establish the correlation between microstructure and fracture toughness, it is of great importance to quantify how an advancing crack interacts with the microstructure at multiple length scales and how microstructure determines a material's fracture toughness through the activation of different fracture mechanisms. Numerous efforts have been made to develop 2D simulation methods to study the crack initiation and propagation in brittle materials [1–4] and metallic polycrystalline materials [5–7]. However, fracture is inherently a 3D problem. Most of these 2D models, which assume plane strain conditions, cannot capture the 3D morphology and orientation of grains, nor do they track crack-material interactions due to nonplanar crack extension.

Over the past few years, the crystal plasticity based finite element method (CPFEM) has been widely used to analyze anisotropic deformation mechanisms in polycrystalline metals [8–10]. This method has also been coupled with the cohesive finite element method (CFEM) to address the material fracture behaviors [11–14]. Currently, most of these models only consider "virtual" idealized microstructures and intergranular fracture along the grain boundaries. None of them provides the capability to explicitly capture both transgranular and intergranular fracture mechanisms and predict fracture toughness for realistic microstructures. The primary challenges lie in the geometrical complexity of 3D microstructures and difficulties to implement such information in finite element modeling.

We propose a multiscale material design framework that includes 3D image based microstructure reconstruction, 3D meshing, and finite element implementation. The 3D microstructures can be reconstructed from actual morphological features and crystallographic orientations, combining experimental investigations involving serial sectioning and electron backscatter diffraction (EBSD) with finite element modeling. For better delineation of grain boundaries and more realistic prediction of crack trajectory, unstructured tetrahedral meshes are employed by using the open source code iso2mesh [15]. Cohesive elements with traction-separation laws are embedded within grains and along the grain boundaries in order to respectively resolve transgranular and intergranular fracture modes. Crystal plasticity is incorporated into a User MATerial Subroutine (UMAT) for use in the commercially available FE software ABAQUS [16]. This modeling framework allows prediction of fracture toughness through explicit simulation of 3D fracture processes in microstructures by calculating the *J*-integral. The methodology gives new insights into the physical aspects of competition between different fracture mechanisms and its correlation with the plastic deformation and crystallographic texture evolution.

3D Microstructure Reconstruction

Voronoi tessellation is a popular technique for generating polycrystalline microstructures due to its simplicity, space-filling nature, and the availability of theoretical results for the topological properties [17,18]. However, microstructures generated in this way are not always consistent with experimental results [19]. To realistically

capture the topological and statistical properties of microstructures, a method for instantiate 3D polycrystalline microstructures is employed. A set of ellipsoidal grains are generated based on predefined distributions of the ratios of the major ellipsoidal axis. These ellipsoids are placed into the space until no more non-overlapping ellipsoids can be placed. The random packing and placement of these ellipsoids follows the algorithm developed by Przybyla [20] and Tschopp [21]. Once every ellipsoidal grain has been randomly placed and oriented, the open space in between is filled by the process of grain growth. The grain growth algorithm starts with one grain and sequences through the rest of the grains, increasing their size in each direction by one pixel at a time. This process repeats itself until every grain reaches its nearest neighbor. After this point, the voxels on either side of the grain boundary no longer evolve in subsequent steps. Once all the free spaces are filled, the 3D microstructure is fully instantiated and its morphological information is stored in a 3D matrix. The exported 2D images are essentially from the generated 3D microstructure. The 2D image series is employed as input for visualization and meshing as required by the open source code iso2mesh [15]. A 2D rendering of ellipsoidal grain packing and the grain structure morphology after grain growth are illustrated in **Fig. 1**.

Using grain equivalent ellipsoids instead of other space filling methods like Voronoi tessellation allows construction of more complex grain morphologies such as elongated grains that are common in rolled ductile metals [22]. A Ti-6Al-4V microstructure with bi-modal grain size distribution is generated using this method with a bi-modal grain size distribution. The grain size is determined by first calculating the new ellipsoid volumes to account for grain growth. The actual grain size cumulative distribution function (CDF) and target CDF for each phase are plotted in **Fig. 2**. This cumulative distribution function can be used to assess how well the final size distribution fits to a log normal distribution function. This algorithm allows explicit control of geometric attributes of the microstructure, such as the volume fraction of each phase, average grain size as well as the grain size distribution. This algorithm allows explicit control of geometric attributes of the microstructure, such as the volume fraction of each phase, average grain size as well as the grain size distribution.

A series of 2D microstructure images generated from the above ellipsoidal packing algorithm are employed as the input for 3D microstructure visualization and meshing. These 2D image series can be experimental data such as serial sectioning

FIG. 1
(a) 2D rendering of ellipsoidal packing algorithm upon initial placement of ellipsoids and (b) 2D rendering of grain structure based on ellipsoidal packing after grain growth.

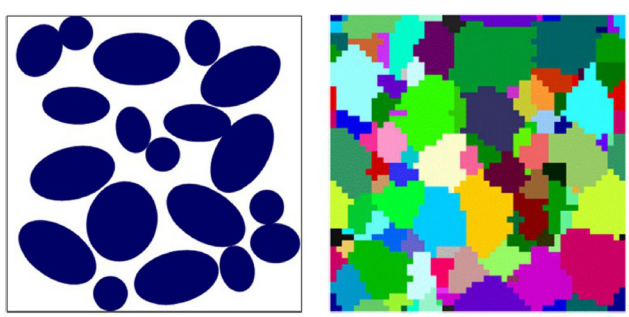

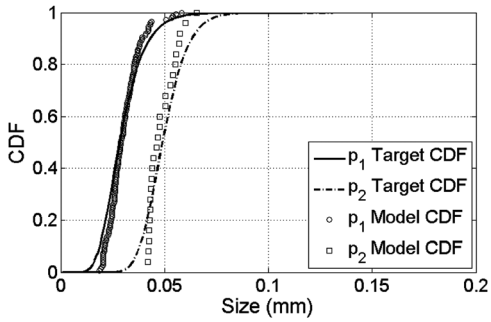

FIG. 2
Target log-normal and fit model distributions of the grain size for the primary α grains (p_1) and the $\alpha + \beta$ grains (p_2).

with EBSD mapping. In order to obtain good delineation of grain boundaries and potential crack trajectories, unstructured tetrahedral meshes are generated by iso2-mesh [15] as illustrated in **Fig. 3**. The output data, including the node coordinates for the generated volumetric mesh and the tetrahedral element information, are used for the finite element implementation.

Finite Element Implementation with 3D Reconstructed Microstructure

An edge-cracked specimen under Mode I tensile loading is modeled as shown in **Fig. 4**. This proposed framework consists of two length scales. The microscopic subgrain scale with refined unstructured meshes has a size of 300 μm by 300 μm by 300 μm. Three-dimensional cohesive elements with 6-node zero thickness (COH3D6) fill the microstructure representation. Constitutive relations for the grains and separation laws for grain boundaries are specified separately. The cohesive relation allows damage and crack surface separation to be considered. Fracture emerges as a natural outcome of the deformation process based on these constitutive laws. Cohesive elements are embedded at the element surfaces both within the grains and along the grain boundaries to resolve transgranular and intergranular fracture. The detailed

FIG. 3 3D microstructure reconstruction, meshing and domain decomposition.

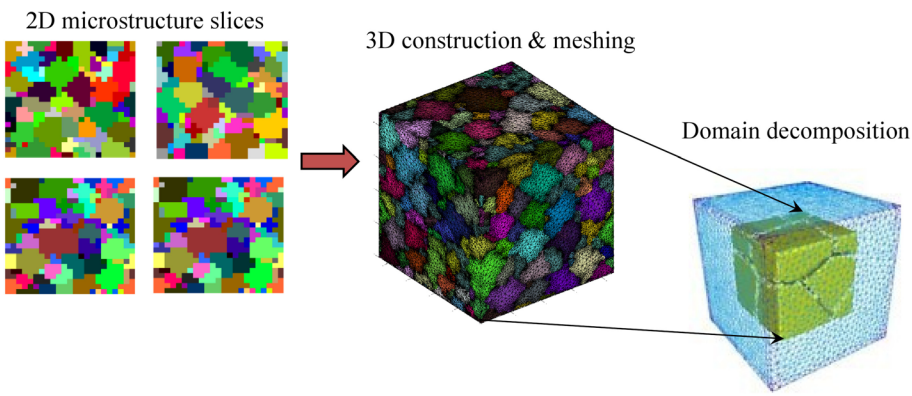

FIG. 4
Specimen configuration used in the analysis.

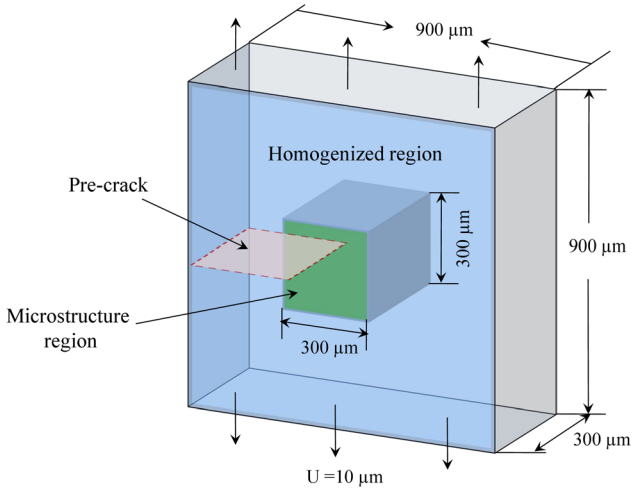

embedding process will be discussed in the following subchapter. The macroscopic region with structured coarse meshes has a size of 900 μm by 900 μm by 300 μm. A boundary displacement $U = 10\,\mu$m is imposed at the top and bottom surfaces to effect Mode I tensile loading. This region does not have any cohesive element and is employed to capture the overall material response at the structure level. We choose elastic parameters $C_{11} = 162400$ MPa, $C_{12} = 92000$ MPa, $C_{13} = 69000$ MPa, $C_{33} = 180700$ MPa, $C_{44} = C_{55} = 46700$ MPa, $C_{66} = 35200$ MPa as reported by Mayeur [23]. The effective shear modulus $\bar{G}$ and bulk modulus $\bar{B}$ in the homogenized region are estimated following the self-consistent method as [24]

$$(1)\quad \begin{cases} \bar{G} = \dfrac{4(C_{11}-C_{13})+2(C_{33}-C_{12})+6(C_{66}+2C_{44})}{60} + \\ \qquad \dfrac{15}{4}\left\{\dfrac{2(C_{11}+C_{12})+C_{33}+4C_{13}}{(C_{11}+C_{12})C_{33}-2C_{13}^2}+\dfrac{3}{C_{11}-C_{12}}+\dfrac{1.5}{C_{66}}+\dfrac{3}{C_{44}}\right\}^{-1} \text{ and} \\ \bar{B} = \dfrac{1}{18}(2C_{11}+C_{33}+2C_{12}+4C_{13}) + \dfrac{C_{33}(C_{11}+C_{12})-2C_{13}^2}{2(C_{11}+C_{12}+2C_{33}-4C_{13})} \end{cases}$$

The effective Young's modulus $\bar{E} = 114.62$ GPa and Poisson's ratio $\bar{\nu} = 0.322$ are calculated according to

$$(2)\quad \begin{cases} \bar{E} = \dfrac{9\bar{B}\bar{G}}{3\bar{B}+\bar{G}} \text{ and} \\ \bar{\nu} = \dfrac{3\bar{B}-2\bar{G}}{6\bar{B}+2\bar{G}} \end{cases}$$

Structural response, such as fracture toughness K_{IC}, is evaluated by calculating the J-integral along an arbitrary contour in this region. Note that the pre-crack locates both within the homogenized and microstructure region. The pre-crack plane introduced in the homogenized region is perpendicular to the applied displacement direction. However, it is impossible to maintain the exactly identical pre-crack plane in the microstructure region since unstructured tetrahedral meshes are employed. To deal with this problem, a pre-crack path that consists of two layers of nodes is

defined to extend the pre-crack to the microstructure as illustrated in **Fig. 5**. These nodes are selected according to their relative distances to the planer pre-crack. In our calculations, a tolerance of $\pm 5\mu$m is considered. These nodes are duplicated and redistributed to elements that share the same surface patches. The introduction of pre-crack facilitates crack initiation and propagation in the microstructure region.

3D COHESIVE ELEMENT INSERTION

Specifying cohesive surfaces for complex 3D microstructure meshes is not a trivial task. The biggest challenge lies in how to effectively deal with the changes in the 3D nodal and elemental connectivities due to the introduction of cohesive surfaces. An algorithm has been developed to automatically insert 3D cohesive elements along grain boundaries and within individual grains, as illustrated in **Fig. 6**. The algorithm includes the following steps: (1) Read the nodal coordinates and element arrangements of the microstructure meshes generated from iso2mesh. (2) Separate the entire node and element information into grain and grain boundary sets, respectively. (3) Define the location where cohesive elements will be inserted. The grain boundary is taken as an example. (4) Sort out all the shared faces and the corresponding element indices within the grain boundary element set. (5) Duplicate the nodes in the shared faces and redistribute the updated node label to the

FIG. 5
Scheme of pre-crack location in the microstructure region.

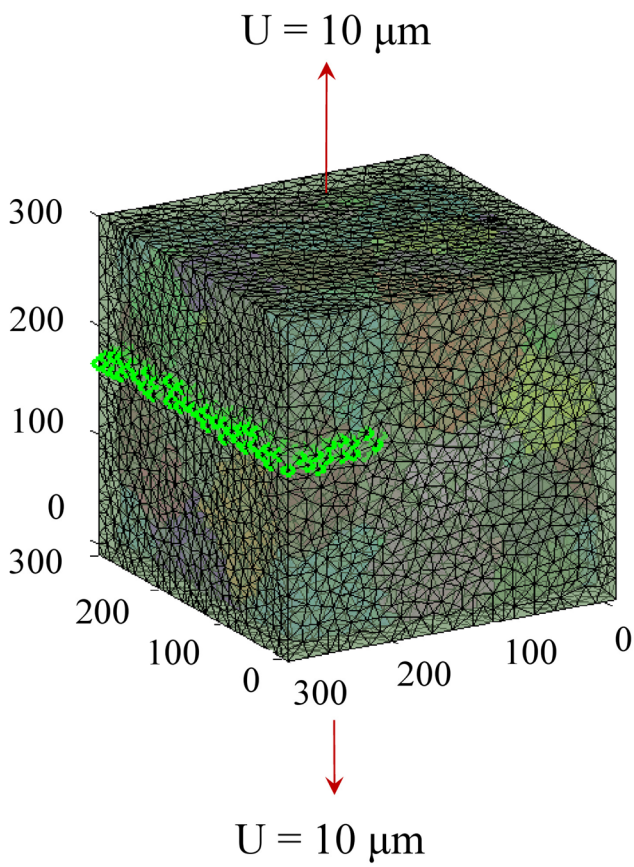

FIG. 6
Illustration of the algorithm for cohesive element insertion.

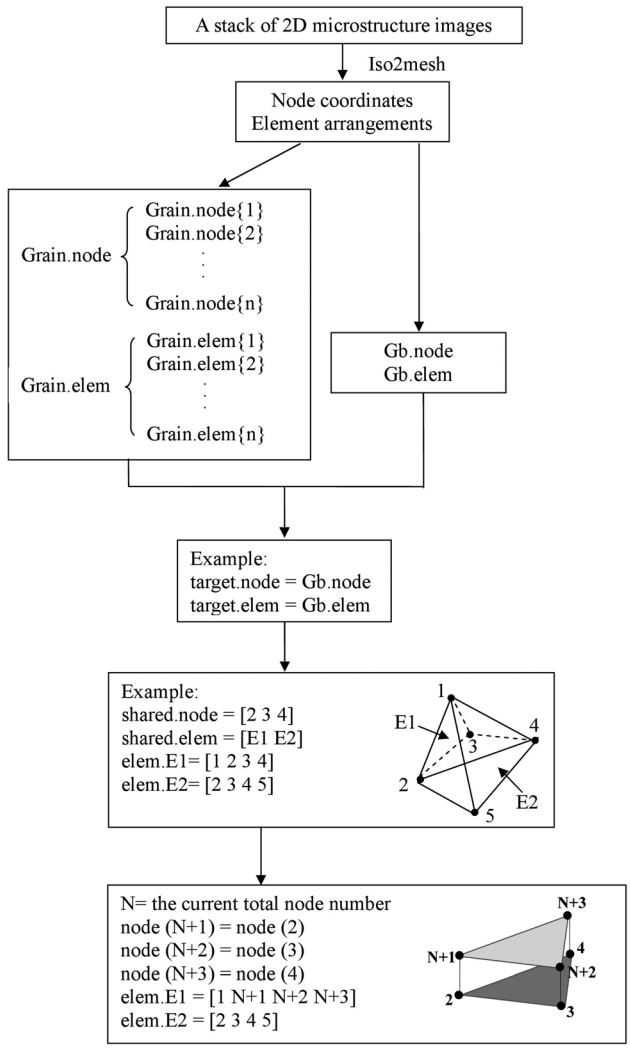

corresponding elements. As illustrated in **Fig. 6**, element 1 and element 2 share the same face with nodes 2, 3, and 4. Assume N is the current total node number. Node N + 1, N + 2, and N + 3 are cloned from node 2, 3, and 4, respectively. When distributing the duplicated nodes to elements (element 1 and element 2 in this case), it is crucial to make sure that the node labels in each element are only allowed to update once. For example, node 2 can be the member of another shared face in addition to face (2 3 4). Once node 2 in element 1 are replaced with node N + 1, it is not allowed to be replaced by another duplicated node afterwards. This duplicated node can only be redistributed to the other element which shared the face. (6) The cohesive element will be generated by connecting the 6 node label. As illustrated in **Fig. 6**, each cohesive element should follow the numbering pattern as [2 3 4 N + 1 N + 2 N + 3].

Generally speaking, each cohesive element is embedded at surfaces shared by two bulk elements. If the two elements belong to different grains, the cohesive element is considered as grain boundary cohesive element. Otherwise, it is assigned as

grain cohesive element. Cohesive elements within each grain are stored in a separate set for different assignment of cohesive laws. The default program will automatically insert cohesive elements everywhere in the microstructure region. The user can also define specific locations for cohesive element insertion, such as the entire grain boundaries, target grains or grain boundaries surrounding the target grains.

Both cohesive elements along grain boundaries and within grains follow the bilinear traction-separation law shown in **Fig. 7**. This is obviously an idealization that can be easily modified to accommodate more detailed and quantitative information regarding; for example, lower cohesive strength or separation energy of intergranular versus transgranular propagation. This law is derived from a potential Φ which is a function of separation vector Δ through a state variable defined as $\lambda = \sqrt{(\Delta_n/\Delta_{nc})^2+(\Delta_t/\Delta_{tc})^2}$. This variable describes the effective instantaneous state of mixed-mode separations. Here, $\Delta_n = \mathbf{n}\cdot\mathbf{\Delta}$ and $\Delta_t=\sqrt{(\Delta_p)^2+(\Delta_q)^2}$ $= \sqrt{[(\mathbf{\Delta}-(\mathbf{\Delta}\cdot\mathbf{n})\mathbf{n})\cdot\mathbf{p}]^2+[(\mathbf{\Delta}-(\mathbf{\Delta}\cdot\mathbf{n})\mathbf{n})\cdot\mathbf{q}]^2} = |\mathbf{\Delta}-(\mathbf{\Delta}\cdot\mathbf{n})\mathbf{n}|$, respectively, denote the normal and tangential components of $\mathbf{\Delta}$, with $\mathbf{n}$ being unit normal and $\mathbf{p}$ and $\mathbf{q}$ being two unit tangential vectors. Note that $\mathbf{n}$, $\mathbf{p}$, and $\mathbf{q}$ are mutually orthogonal to each other and form a right-handed triad. Δ_{nc} is the critical normal separation at which the cohesive strength of an interface vanishes under conditions of pure normal deformation ($\Delta_t = 0$). Similarly, Δ_{tc} is the critical tangential separation at which the cohesive strength of an interface vanishes under conditions of pure shear deformation ($\Delta_n = 0$). $T_{\max}$ represents the maximum traction that the cohesive element can sustain at the onset of irreversible separation.

In order to account for the irreversibility of separations, a parameter $\eta = \max\{\eta_0, \lambda_{ul}\}$ is defined. As illustrated in **Fig. 7**, η_0 is the initial value of η which defines the stiffness of the original undamaged cohesive surface, while λ_{ul} is the hitherto maximum value of λ at which an unloading process was initiated. It should be noted that λ_{ul} is associated with the onset of an unloading event and is not necessarily the hitherto maximum value of λ. λ_{ul} represents the current (reduced) stiffness of the cohesive surfaces after damage and unloading have occurred. Furthermore, η_0 represents the characteristic value of effective separation λ at which the effective traction σ for a cohesive surface pair reaches the strength $T_{\max}$ of the undamaged surface. λ_{ul} stands for the critical level of λ at which σ reaches the reduced strength $T_{\max}(1-\eta)/(1-\eta_0)$ of the hitherto damaged cohesive surface pair. As indicated in **Fig. 7**, separation occurs elastically and the cohesive energy stored (work done in

FIG. 7
Bilinear traction-separation law.

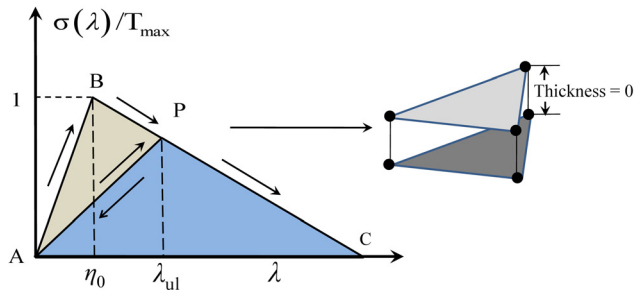

causing separation) is fully recoverable between A and B ($0 \leq \lambda \leq \eta_0$). Damage in the form of microcracks and other small-scale defects does not occur. Between B and C ($\eta_0 \leq \lambda \leq 1$), material degradation causes progressive reduction in the strength of the cohesive surfaces. This represents a phenomenological account of the effects of microcracks and other defects not explicitly modeled in the CFEM model. Unloading from any point P follows path PA and subsequent reloading follows AP and then PC. Part of the work expended on causing the separation in this regime is irreversible, as indicated by the hysteresis loop ABP which implies dissipation during the softening process. Correspondingly, there is a decrease in the maximum tensile strength of the cohesive surface. This is reflected in the elastic reloading of the interface along AP and further softening along path PC.

CRYSTAL PLASTICITY FORMULATION

Plastic deformation in metals is a manifestation of dislocation motion and interaction at the microscopic scale. The details are intimately related to the crystallographic structure of the material as well as the current state of the microstructure. Macroscopic models of plasticity lack the ability to link these fundamental mechanisms to the bulk material response without very substantial experimental characterization. Many formulations of constitutive laws for the elastic–plastic deformation of single and polycrystals have long been proposed [25–30]. The basic premise of these theories is that macroscopic plastic deformation is related to the cumulative process of slip system shearing relative to the lattice. This methodology provides a physical link between the processes at different length scales. The two basic components of crystal plasticity model are the kinematic and kinetic relations.

The multiplicative decomposition of the total deformation gradient is given by

$$\mathbf{F} = \mathbf{F}^e \cdot \mathbf{F}^p \tag{3}$$

where:

$\mathbf{F}^e$ = the elastic deformation gradient representing the elastic stretch and rotation of lattice, and

$\mathbf{F}^p$ = the plastic deformation gradient describing the collective effects of dislocation motion along the active slip planes relative to a fixed lattice in the reference configuration.

Unit vectors $\boldsymbol{s}_0^\alpha$ and $\boldsymbol{n}_0^\alpha$ denote the slip direction and the slip plane normal direction, respectively, for the α^{th} slip system in the undeformed configuration. The resolved shear stress on each slip system is related to the Cauchy stress tensor σ according to

$$\tau^\alpha = \sigma{:}(\boldsymbol{s}^\alpha \otimes \boldsymbol{n}^\alpha) \tag{4}$$

where the slip vectors have been rotated into the current configuration. Under the application of the resolved shear stress, the shearing rates $\dot{\gamma}^\alpha$ on the slip systems are related to the plastic velocity gradient in the intermediate configuration according to

$$\mathbf{L}^p = \sum_\alpha \dot{\gamma}^\alpha \mathbf{s}_0^\alpha \otimes \mathbf{n}_0^\alpha \tag{5}$$

with $\dot{\gamma}^\alpha$ ascribed to follow the rate-dependent flow rule as

$$\dot{\gamma}^{\alpha} = \dot{\gamma}_0 \left\langle \frac{\tau^{\alpha} - \chi^{\alpha}}{g^{\alpha}} \right\rangle^{m} \operatorname{sgn}(\tau^{\alpha} - \chi^{\alpha}) \tag{6}$$

where:

m = the inverse strain rate sensitivity exponent, and

g^{α} and χ^{α} = drag stress and back stress, respectively, on the α^{th} slip system.

These quantities evolve according to

$$\begin{cases} \dot{g}^{\alpha} = H \sum_{\beta=1} q^{\alpha\beta} \left| \dot{\gamma}^{\beta} \right|, \text{ and} \\ \dot{\chi}^{\alpha} = A_{kin} \dot{\gamma}^{\alpha} - A_{dyn} \chi^{\alpha} \left| \dot{\gamma}^{\alpha} \right| \end{cases} \tag{7}$$

Here, $q^{\alpha\beta}$ is the latent hardening coefficient, H, A_{kin}, and A_{dyn} are the isotropic hardening, kinematic hardening and dynamic recovery coefficients, respectively. These non-linear coupled differential equations are solved using UMAT [22].

GENERATION OF MESH TIE CONSTRAINT

Calculation of the J-integral in the homogenized region requires a closed contour connecting the upper and lower crack surfaces. It is very difficult to define contours if the homogenized region is meshed with unstructured elements as in the microstructure. One possible way to address this problem is to use structured tetrahedral meshes in the homogenized region and generate a transitional region to connect the two types of meshes together. However, this method requires very sophisticated algorithms and may pose the challenge to change the size of the model when different mesh density is employed in the microstructure region. Apparently, the transitional region will increase as the discrepancy of mesh density between the two mesh regions increases. The size dependency of microstructure mesh density precludes the application of this method.

We employ the mesh tie constraint to assemble the two regions with different mesh types and densities as illustrated in **Fig. 8**. This constraint requires no conformity of nodal connectivity between the two regions. It circumvents the problem with acceptable accuracy. As illustrated for a 2D problem in **Fig. 9**, there is only a

FIG. 8
Model assembly between the microstructure and homogenized region through mesh tie constraint.

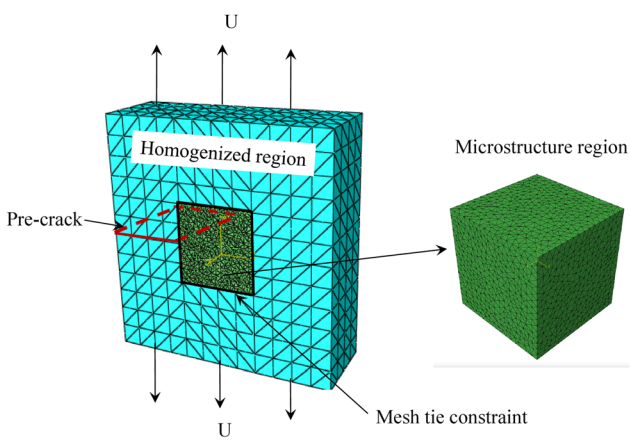

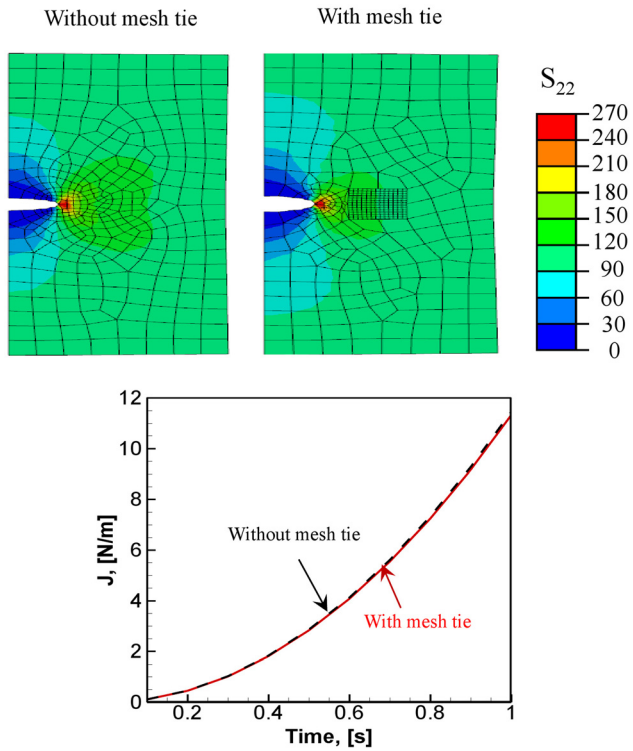

FIG. 9
Effect of mesh tie constraint on the calculated J values.

very minor difference between the J values for cases with and without the mesh tie constraint. It should be noted that iso2mesh cannot generate perfect microstructure meshes with smooth exterior surfaces and sharp vertices as shown in **Fig. 10**. If the two regions cannot be seamlessly attached, the energy loss caused by the gap will significantly influence the accuracy of calculation. We develop an innovative algorithm to generate a shell mesh, which is around the unsmoothed microstructure block to ensure proper node and element connectivity to the surrounding homogenized region. Now the two regions can be seamlessly assembled and be preceded to finite element analysis in ABAQUS.

Results and Discussions

A microstructure 300 μm by 300 μm by 300 μm in size is employed in the following calculation. It is inserted into the finite element model using the methodology discussed in the previous section. A displacement of $U = 10\,\mu$m is applied on both the upper and lower surfaces of the model, as illustrated in **Fig. 4**.

For ductile materials, two major competitions are at work. One is the competition between different fracture mechanisms (for example, transgranular fracture versus intergranular fracture). The other competition is between material deformation (inelasticity) and crack face generation. In this paper, we focus on how heterogeneous grain deformation affects crack initiation and propagation. To simplify the analysis, we assume all grains share the same mechanical properties, except initial

FIG. 10 Shell mesh region around the unsmoothed microstructure mesh.

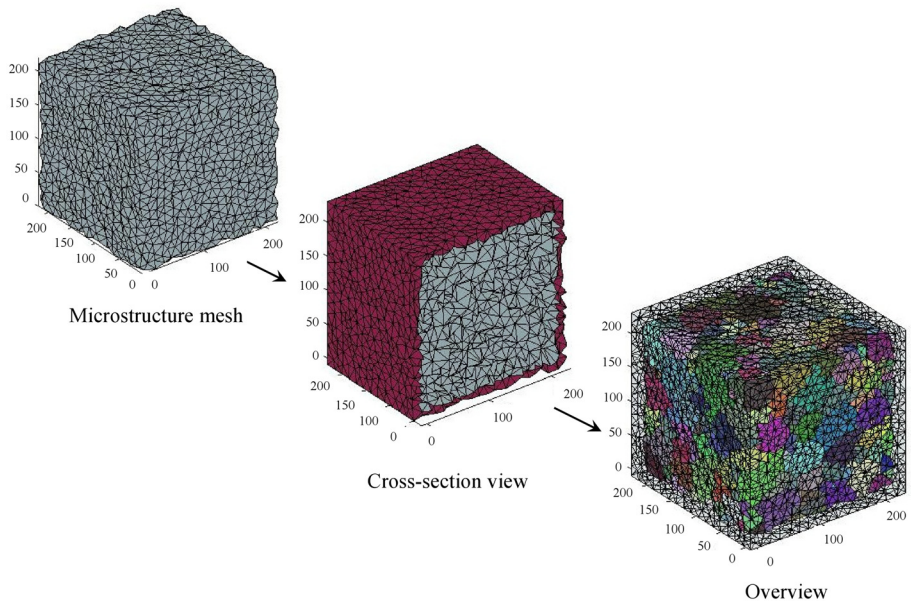

orientations which are randomly assigned. Besides, the cohesive elements in the grains and grain boundaries follow the same traction-separation law, so that they are equally likely to fracture on one account. Under conditions of small-scale yielding, the fracture energy Φ of Ti-6Al-4V is $\Phi = J = (1-\nu^2)K_{IC}^2/E = 9.58\,\mathrm{KJ/m^2}$, with the Young's modulus $E = 114.62\,\mathrm{GPa}$, Poisson's ratio $\nu = 0.322$, and the fracture toughness $K_{IC} = 35\,\mathrm{MPa}\sqrt{\mathrm{m}}$. The maximum traction $T_{\max}$ is obtained from $T_{\max} = (2\Phi/\Delta_{nc}) = (2\Phi/\alpha\Delta_{tc})$, where α is defined as Δ_{nc}/Δ_{tc} and is assumed to be 1. In order for the cohesive surfaces to achieve complete debonding, both the normal and shear separations should not exceed the element size. Otherwise, the cohesive surfaces would not fully debond and the damage cannot be considered true crack formation. In our model, $\Delta_{nc} = \Delta_{tc} \in (1, 10)\,\mu\mathrm{m}$ is a reasonable range for the separation. The corresponding range of $T_{\max}$ calculated from the above relations is 1.916–19.16 GPa. For the specific case considered, $T_{\max} = 16\,\mathrm{GPa}$ is employed for all three directions.

It is noted from **Fig. 11(*a*)** that multiple cracks are observed in the microstructure region. When mapping the deformed nodal coordinates to the grain arrangement illustrated in **Fig. 11(*b*)**, we notice that transgranular fracture is the dominant failure mode. Even though the grains and grain boundaries are equally likely to fracture (as the chosen condition for the analysis carried out here), the cracks tend to go through the grains instead of following the grain boundaries. Besides, most of the cracks do not follow the plane of the pre-crack and instead initiate away from it. To shed light on this issue, a calculation is carried out without the pre-crack and the cohesive elements in the microstructure. The result is shown in **Fig. 11(c)**. Again, cracks tend to nucleate and propagate in grains with lower levels of plastic deformation. The excessive strain energy which cannot be dissipated through plastic deformation has to be released through surface creation. The propagation of the pre-crack is temporarily

FIG. 11 (a) Illustration of crack propagation in the microstructure, (b) mapping of deformed configuration in the microstructure, and (c) anisotropic deformation in the microstructure region without pre-crack and cohesive elements.

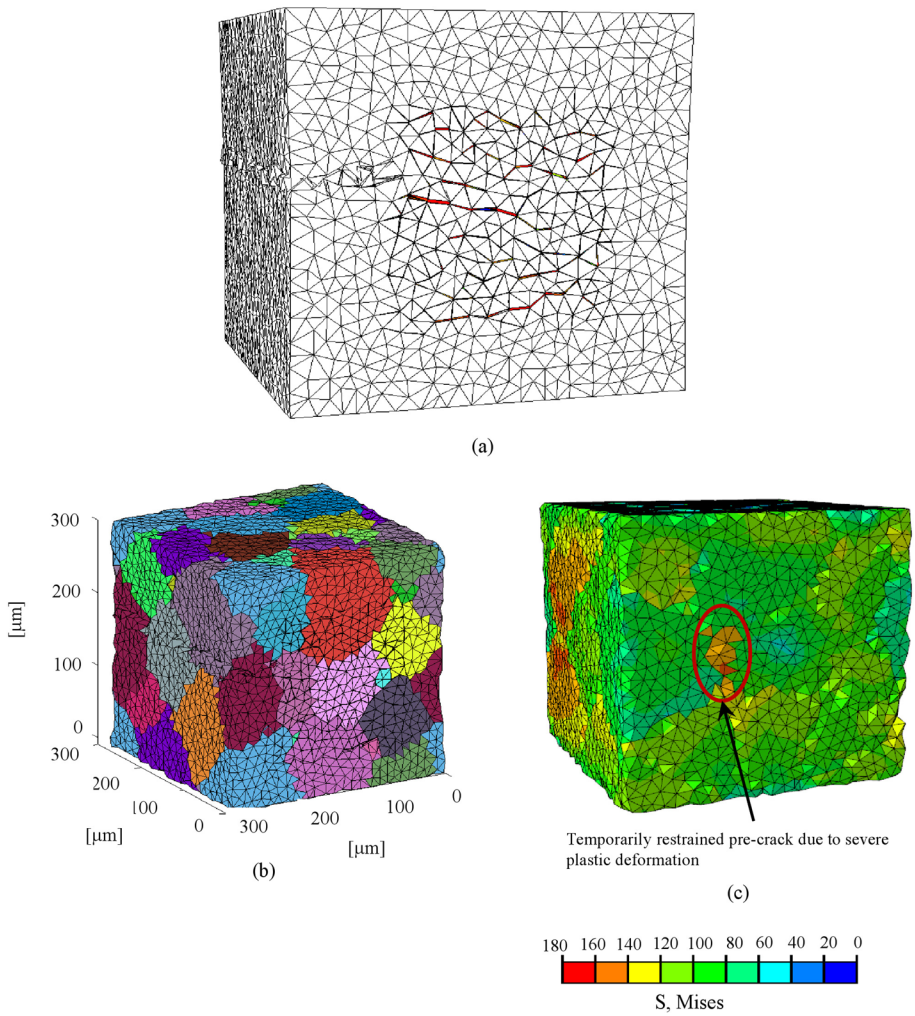

restrained due to the significant plastic deformation in front of the crack-tip as illustrated in **Fig. 11(c)**. Instead, microcracks nucleate and propagate into grains with less plastic deformation. This example well explains the competition between material deformation and crack formation. Further correlation between fracture toughness, grain orientation, and grain size distribution can be established by using the framework developed here. More systematic studies regarding the above issues will be discussed in the future publications.

Conclusion

A cohesive finite element based multiscale framework is developed to simulate crack initiation and propagation in 3D polycrystalline microstructures. Crystal plasticity is incorporated into the constitutive relations to capture how anisotropic deformation

and texture evolution affect the crack propagation and the activation of different fracture mechanisms. The methodology we proposed provides a way to reconstruct 3D microstructures from experimental data. It also allows the morphological and crystallographic information of the microstructure to be implemented in the finite element analysis, facilitating the ability to tailor microstructure to enhance fracture toughness.

ACKNOWLEDGMENTS

This work was funded by the Center for Computational Materials Design (CCMD), a joint National Science Foundation (NSF) Industry/University Cooperative Research Center at Penn State (IIP-1034965) and Georgia Tech (IIP-1034968).

References

[1] Xu, X. P. and Needleman, A., "Numerical Simulations of Fast Crack-Growth in Brittle Solids," *J. Mech. Phys. Solids*, Vol. 42, 1994, pp. 1397–1434.

[2] Zhai, J., Tomar, V. and Zhou, M., "Micromechanical Simulation of Dynamic Fracture Using the Cohesive Finite Element Method," *J. Eng. Mater. Technol.*, Vol. 126, 2004, pp. 179–191.

[3] Li, Y. and Zhou, M. "Prediction of Fracture Toughness of Ceramic Composites as Function of Microstructure: I. Numerical Simulations," *J. Mech. Phys. Solids*, Vol. 61, 2013, pp. 472–488.

[4] Li, Y. and Zhou, M. "Prediction of Fracturess Toughness of Ceramic Composites as Function of Microstructure: II. Analytical Model," *J. Mech. Phys. Solids*, Vol. 61, 2013, pp. 489–503.

[5] Guo, X., Chang, K., Chen, L. Q. and Zhou, M., "Determination of Fracture Toughness of AZ31 Mg Alloy Using the Cohesive Finite Element Method," *Eng. Fract. Mech.*, Vol. 96, 2012, pp. 401–415.

[6] Meyers, M. A., Mishra, A. and Benson, D. J., "Mechanical Properties of Nanocrystalline Materials," *Prog. Mater. Sci.*, Vol. 51, 2006, pp. 427–556.

[7] Hao, S., Lin, H., Binomiemi, R. R., Combs, D. M. G. and Fett, G., "A Multi-Scale Model of Intergranular Fracture and Computer Simulation of Fracture Toughness of a Carburized Steel," *Comput. Mater. Sci.*, Vol. 48, 2010, pp. 241–249.

[8] Mayeur, J. R., McDowell, D. L. and Neu, R. W., "Crystal Plasticity Simulations of Fretting of Ti-6Al-4V in Partial Slip Regime Considering Effects of Texture," *Comput. Mater. Sci.*, Vol. 41, 2008, pp. 356–365.

[9] Clayton, J. D. and McDowell, D. L., "Homogenized Finite Elastoplasticity and Damage: Theory and Computations," *Mech. Mater.*, Vol. 36, 2004, pp. 799–824.

[10] Li, S. Y., Van Houtte, P., and Kalidindi, S. R., "A Quantitative Evaluation of the Deformation Texture Predictions for Aluminium Alloys from Crystal Plasticity Finite Element Method," *Modell. Simul. Mater. Sci. Eng.*, Vol. 12, 2004, pp. 845–870.

[11] Siddiq, A. and Rahimi, S., "A Multiscale Constitutive Model for Intergranular Stress Corrosion Cracking in Type 304 Austenitic Stainless Steel," *International*

Symposium on Dynamic Deformation and Fracture of Advanced Materials (D2fam 2013), Vol. 451, Loughborough, United Kingdom, Sept 9–11, 2013.

[12] Zhang, P., Karimpour, M., Balint, D. and Lin, J., "Cohesive Zone Representation and Junction Partitioning for Crystal Plasticity Analyses," *Int. J. Numer. Methods Eng.*, Vol. 92, 2012, pp. 715–733.

[13] Siddiq, A. and Schmauder, S., "Multiscale Simulation of Metal/Ceramic Interface Fracture," *Iutam Symposium on Multi-Functional Material Structures and Systems*, Vol. 19, 7th ed., B. Dattaguru, S. Gopalakrishnan, and V. K. Aatre, Eds., 2010, pp. 343–355.

[14] Grujicic, M., Cao, G. and Batchu, S., "Crystal Plasticity-Based Finite Element Analysis of Deformation and Fracture of Polycrystalline Lamellar Gamma-Tial + alpha(2)-Ti(3)al Alloys," *J. Mater. Sci.*, Vol. 38, 2003, pp. 307–322.

[15] Fang, Q. Q. and Boas, D. A., "Tetrahedral Mesh Generation from Volumetric Binary and Gray-Scale Images," *Proceedings of the 2009 IEEE International Symposium on Biomedical Imaging: From Nano to Macro*, Vols. 1 and 2, Boston, MA, June 28–July 1, 2009, pp. 1142–1145.

[16] *ABAQUS 6-12*. (2012). Simulia, Providence, RI.

[17] Leonardi, A., Scardi, P. and Leoni, M., "Realistic nano-Polycrystalline Microstructures: Beyond the Classical Voronoi Tessellation," *Philos. Mag.*, Vol. 92, 2012, pp. 986–1005.

[18] Luther, T. and Könke, C., "Polycrystal Models for the Analysis of Intergranular Crack Growth in Metallic Materials," *Eng. Fract. Mech.*, Vol. 76, 2009, pp. 2332–2343.

[19] Xu, T. and Li, M., "Topological and Statistical Properties of a Constrained Voronoi Tessellation," *Philos. Mag.*, Vol. 89, 2009, pp. 349–374.

[20] Przybyla, C. P. and McDowell, D. L., "Simulation-Based Extreme Value Marked Correlations in Fatigue of Advanced Engineering Alloys," *Proc. Eng.*, Vol. 2, 2010, pp. 1045–1056.

[21] Tschopp, M., Personal Communication, 2009.

[22] Przybyla, C. P. and McDowell, D. L., "Simulated Microstructure-Sensitive Extreme Value Probabilities for High Cycle Fatigue of Duplex Ti–6Al–4V," *Int. J. Plast.*, Vol. 27, 2011, pp. 1871–1895.

[23] Mayeur, J. R. and McDowell, D. L., "A Three-Dimensional Crystal Plasticity Model for Duplex Ti-6Al-4V," *Int. J. Plast.*, Vol. 23, 2007, pp. 1457–1485.

[24] Sisodia, P. and Verma, M. P., "Polycrystalline Elastic-Moduli of Some Hexagonal and Tetragonal Materials," *Phys. Stat. Solidi A—Appl. Res.*, Vol. 122, 1990, pp. 525–534.

[25] Taylor, G. I., "Plastic Strain in Metals," *J. Inst. Metals*, Vol. 62, 1938, pp. 307–324.

[26] Hill, R. and Rice, J. R., "Constitutive Analysis of Elastic-Plastic Crystals at Arbitrary Strain," *J. Mech. Phys. Solids*, Vol. 20, 1972, pp. 401–413.

[27] Asaro, R. J. and Rice, J. R., "Strain Localization in Ductile Single-Crystals," *J. Mech. Phys. Solids*, Vol. 25, 1977, pp. 309–338.

[28] Peirce, D., Asaro, R. J. and Needleman, A., "An Analysis of Nonuniform and Localized Deformation in Ductile Single-Crystals," *Acta Metall.*, Vol. 30, 1982, pp. 1087–1119.

[29] McGinty, R. D. and McDowell, D. L., "Application of Multiscale Crystal Plasticity Models to Forming Limit Diagrams," *Trans. ASME J. Eng. Mater. Technol.*, Vol. 126, 2004, pp. 285–291.

[30] Cuitino, A. M. and Ortiz, M., "Computational Modeling of Single-Crystals," *Modell. Simul. Mater. Sci. Eng.*, Vol. 1, 1993, pp. 225–263.